

# Chain-length dependent growth dynamics of n-alkanes on silica investigated by energy-dispersive x-ray reflectivity *in situ* and in real-time

C. Weber,<sup>1</sup> C. Frank,<sup>2</sup> S. Bommel,<sup>1,3</sup> T. Rukat,<sup>1</sup> W. Leitenberger,<sup>4</sup> P. Schäfer,<sup>1</sup>  
F. Schreiber,<sup>2</sup> and S. Kowarik<sup>1,a)</sup>

<sup>1</sup>*Institut für Physik, Humboldt-Universität zu Berlin, Newtonstr. 15, 12489 Berlin, Germany*

<sup>2</sup>*Institut für Angewandte Physik, Universität Tübingen, Auf der Morgenstelle 10, 72076 Tübingen, Germany*

<sup>3</sup>*Deutsches Elektronen-Synchrotron (DESY), Notkestraße 85, 22607 Hamburg, Germany*

<sup>4</sup>*Institut für Physik, Universität Potsdam, Karl-Liebknecht-Strasse 24/25, 14476 Potsdam-Golm, Germany*

(Received 21 March 2012; accepted 3 May 2012; published online 31 May 2012)

We compare the growth dynamics of the three n-alkanes  $C_{36}H_{74}$ ,  $C_{40}H_{82}$ , and  $C_{44}H_{90}$  on  $SiO_2$  using real-time and *in situ* energy-dispersive x-ray reflectivity. All molecules investigated align in an upright-standing orientation on the substrate and exhibit a transition from layer-by-layer growth to island growth after about 4 monolayers under the conditions employed. Simultaneous fits of the reflected intensity at five distinct points in reciprocal space show that films formed by longer n-alkanes roughen faster during growth. This behavior can be explained by a chain-length dependent height of the Ehrlich-Schwoebel barrier. Further x-ray diffraction measurements after growth indicate that films consisting of longer n-alkanes also incorporate more lying-down molecules in the top region. While the results reveal behavior typical for chain-like molecules, the findings can also be useful for the optimization of organic field effect transistors where smooth interlayers of n-alkanes without co-existence of two or more molecular orientations are required. © 2012 American Institute of Physics. [<http://dx.doi.org/10.1063/1.4719530>]

## I. INTRODUCTION

Because of their simple structure linear alkanes (n-alkanes) have frequently been used as model systems for carbon based chain-like molecules to study their behavior at varying temperatures or specific interfaces.<sup>1–3</sup> In addition to that, n-alkane films are technologically relevant as protective layers and lubricants in numerous applications ranging from medicine to molecular electronics.<sup>4,5</sup> It is possible to control, for instance, the wettability and chemical reactivity of surfaces using self-assembled monolayers (ML) of n-alkane derivatives such as alkanethiols.<sup>6,7</sup> In the case of molecular electronic devices, small structural changes within one layer can result in drastically different electronic properties of the surrounding layers. For example, recently a passivation layer of n-tetratetracontane ( $C_{44}H_{90}$ ) helped to remove electron traps on a silicon oxide surface and therefore increased the charge carrier mobility of an organic field effect transistor by one order of magnitude.<sup>5,8</sup>

Experiments in the past have shown that even minimal changes of the chain-length of n-alkanes can lead to large changes of molecular orientation and completely different thermodynamic behavior. Rotator phases have been found,<sup>9,10</sup> i.e., n-alkanes with certain chain-lengths undergo first-order phase transitions upon heating. Another example is the odd-even effect,<sup>11,12</sup> where monolayers of n-alkanes adsorb in specific geometries on substrates and have different boiling points depending on whether they have an odd or even number of carbon chain segments.

While in the regime of shorter n-alkanes (carbon number  $n \leq 22$ ), it has been observed that molecules with less carbon atoms form a more disordered molecular structure, less is known about the multilayer ordering behavior of n-alkanes with medium length ( $36 \leq n \leq 50$ ). Parameters such as the persistence length and the intramolecular degrees of freedom of the molecules are supposed to play a major role in the film growth process of longer and thus more flexible n-alkanes.<sup>13,14</sup> We use three different n-alkanes ( $C_nH_{2n+2}$ :  $= C_n$ ) shown in Figure 1(a), with even carbon numbers, namely, n-hexatriacontane ( $C_{36}H_{74}$ ), n-tetracontane ( $C_{40}H_{82}$ ), and n-tetratetracontane ( $C_{44}H_{90}$ ) to study the influence of chain-length on molecular growth and thin film structure.

While the system has been studied as a model for wetting and dewetting, we emphasize that growth is a kinetic process with a multitude of physical processes happening at the same time. In this case, we are in particular interested in the role of interlayer-transport of molecules in the roughening regime. Interlayer-transport denotes the process of molecules hopping from one layer into the next lower layer during organic thin film growth (see Figure 1(c)). This process can either be governed by the diffusivity of molecules or by the height of the energy barrier that molecules have to overcome when hopping from one into another layer (Ehrlich-Schwoebel barrier,<sup>15–17</sup> Figure 1(b)). Optical and x-ray real-time methods are particularly suited to monitor the growth dynamics such as transitions in growth mode, interlayer-transport, and roughening, since the growth of organic thin films usually is a non-equilibrium process.<sup>18–22</sup> After the growth process has stopped, many organic systems undergo structural changes, for example, dewetting.<sup>23,24</sup>

<sup>a)</sup>Electronic mail: stefan.kowarik@physik.hu-berlin.de.

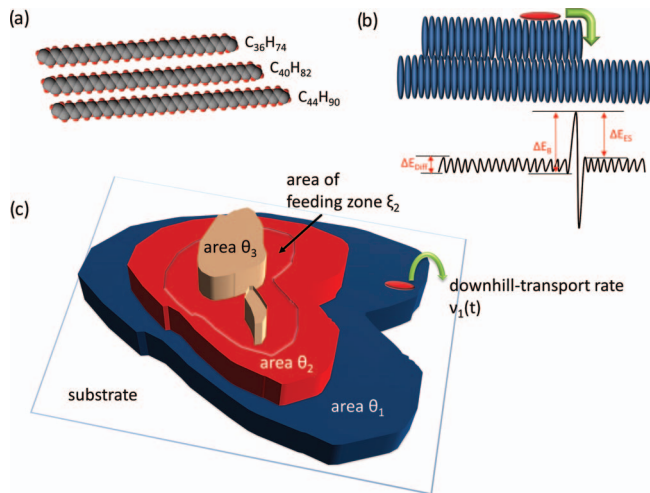


FIG. 1. (a) Atomic structure of n-tetratetracontane (C<sub>44</sub>), n-tetracontane (C<sub>40</sub>), and n-hexatriacontane (C<sub>36</sub>). (b) Sketch of the Ehrlich-Schwoebel barrier for the case of a single molecule diffusing across a layer of upright standing molecules.  $\Delta E_{\text{Diff}}$  denotes the diffusion barrier that molecules have to overcome when moving from one spot to another spot nearby within the same layer,  $\Delta E_{\text{B}}$  marks the step-edge barrier that molecules have to overcome when diffusing from one layer into the next lower layer. The Ehrlich-Schwoebel barrier is then defined as the difference  $\Delta E_{\text{ES}} = \Delta E_{\text{B}} - \Delta E_{\text{Diff}}$ . (c) Illustration of the growth process.  $\theta_1$ ,  $\theta_2$ , and  $\theta_3$  denote the layer coverage of the first, the second, and the third layer.  $\xi_2$  denotes the feeding zone of the second layer, and  $v_1$  describes the downhill-transport of molecules from the second into the first layer.

In this work, we show that in the case of n-alkanes on SiO<sub>2</sub>, a smaller interlayer-transport leads to a greater roughness of the final film. Films consisting of longer molecules exhibit faster roughening in multilayer growth. While all three films mainly consist of upright standing molecules ( $\sigma$ -orientation), a chain-length dependent amount of lying-down molecules ( $\lambda$ -orientation) is found within the upper region of each film. The x-ray measurements point to the fact that longer molecules form a higher percentage of  $\lambda$ -orientation.

## II. EXPERIMENTAL

The alkanes n-hexatriacontane, n-tetracontane, and n-tetratetracontane were bought from Sigma Aldrich with an analytical standard purity grade (Supelco). The films were grown under high vacuum conditions (pressure within chamber  $\leq 10^{-7}$  mbar) on silicon (100) wafers covered by native SiO<sub>2</sub>. The substrates were cleaned in an ultrasonic bath in three steps, first using acetone, then 2-propanol (>99.9%), and finally ultrapure water.

The molecules were evaporated from a Knudsen cell attached above the substrate.<sup>25</sup> The growth rate was set to 10 Å/min as monitored by a crystal quartz microbalance. In the case of C<sub>44</sub>, the growth rate of the first two monolayers dropped temporarily below 3 Å/min, but during the growth of the second monolayer it was increased and stabilized to 10 Å/min again. The substrate temperature was measured at two spots inside and outside the sample holder and was set to 34 °C (average of temperatures at both spots). It is known that structural rearrangements can occur already below

the melting temperature for n-alkanes.<sup>26</sup> In the case of the shortest molecule C<sub>36</sub>, such effects have been observed only for temperatures above 60 °C ( $T_m \approx 80$  °C). Therefore, while we cannot rule out that they contribute to some extent, these premelting effects should not have a significant influence on the structure at 35 °C. The real-time x-ray reflectivity (XRR) measurements were performed using a portable UHV chamber<sup>27</sup> at the BESSY II synchrotron source at the energy-dispersive reflectivity (EDR) beamline.<sup>28</sup> The technique of energy dispersive detection makes it possible to measure the x-ray reflectivity within a wide  $q$ -range without moving the sample and can thus provide good temporal resolution.<sup>29,30</sup> The white synchrotron x-ray beam (5–30 keV) was reflected on the sample and detected by an energy dispersive *Roentec Xflash 1000* detector that provided an energy resolution of about 200 eV. The time-resolution of about 30 s was limited by the intensity of the scattered signal needed for a signal-to-noise ratio of >100. The angle of incidence was set to 0.386°. At this fixed angle of incidence, the monolayer-Bragg reflection (002) of C<sub>36</sub> can be found at a photon energy of 19.6 keV, while in the case of C<sub>40</sub>, the (002)-Bragg reflection appears at 17.7 keV and for C<sub>44</sub> at 16.2 keV. In this way, it was possible to use simultaneously photon energies between 8 and 20 keV that provided the highest flux to monitor the region between the monolayer-anti-Bragg point and the monolayer-Bragg-point in the reciprocal space.

In order to measure a wide energy interval of reflected x-rays with a single x-ray detector simultaneously, we had to adapt the energy spectrum and the intensity of the incoming beam by attenuators made of aluminum.<sup>28</sup> The reflectivity data were normalized for each set of absorbers with the corresponding spectrum of the direct beam. After the real-time runs, the samples were checked for x-ray beam damage by comparing the reflectivity at pristine and exposed spots. Deviations of less than 1% were visible so that we conclude that our results are not significantly influenced by beam damage within our accuracy. The XRR and grazing incidence x-ray diffraction (GIXD) measurements of the final film structure were performed on a lab based diffractometer with a Cu- $K_{\alpha}$  rotating anode source. The angle of incidence was set to 0.17° for the GIXD measurements and the vertical gap of the detector slits gave an acceptance angle of  $\alpha_f < 1^\circ$ . Post-growth atomic force microscopy (AFM) images were measured in tapping mode with a JPK Nanowizard II.

## III. RESULTS AND DISCUSSION

The as-grown structure for films of thicknesses between 90 and 120 nm has been investigated with XRR and GIXD (see Figure 2(b)). All three n-alkanes show similar in-plane unit cell structures whereas the out-of-plane lattice spacing differs depending on the length of the molecules, indicating mainly upright-standing molecules with respect to the substrate surface. According to the literature,<sup>2,31</sup> coexistence of an orthorhombic ( $a = 4.96$  Å,  $b = 7.42$  Å,  $c = 95.14$  Å,  $\alpha = \beta = \gamma = 90^\circ$ ) and a monoclinic unit cell ( $a = 5.572$  Å,  $b = 7.420$  Å,  $c = 45.93$  Å,  $\alpha = \beta = 90^\circ$ ,  $\beta = 113^\circ$ ) has been observed for C<sub>36</sub>, while only orthorhombic unit cells

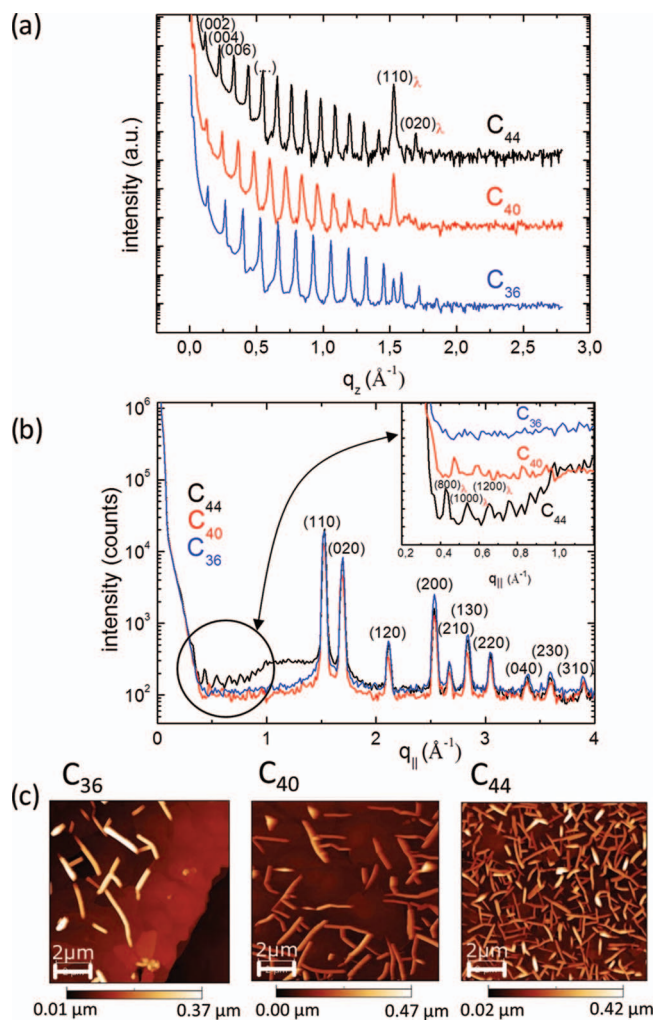


FIG. 2. (a) X-ray reflectivity, (b) grazing incidence x-ray diffraction, and (c) atomic force microscopy scans of  $C_{36}$ ,  $C_{40}$ , and  $C_{44}$  (shown area  $10 \times 10 \mu\text{m}$ ). The lattice spacings as extracted from the XRR measurements for the monolayer thickness are  $d = 47.8 \text{ \AA}$  for  $C_{36}$ ,  $d = 52.8 \text{ \AA}$  for  $C_{40}$ , and  $d = 57.6 \text{ \AA}$  for  $C_{44}$ .

have been observed for  $C_{40}$  ( $a = 4.966 \text{ \AA}$ ,  $b = 7.430 \text{ \AA}$ ,  $c = 93.680 \text{ \AA}$ ,  $\alpha = \beta = \gamma = 90^\circ$ ) and  $C_{44}$  ( $a = 4.982 \text{ \AA}$ ,  $b = 7.427 \text{ \AA}$ ,  $c = 102.740 \text{ \AA}$ ,  $\alpha = \beta = \gamma = 90^\circ$ ) thus far.

The observed  $(hk0)$ -reflections in our GIXD data in Figure 2(b) would not be consistent with a deviation from the  $90^\circ$ -angles of an orthorhombic unit cell by more than  $3^\circ$ . The indexing of the Bragg reflections is in agreement with an orthorhombic  $Pca2_1$  unit cell (see Table I) as it has been observed before in bulk and on Si(100) for  $C_{36}$  and shorter molecules. From our data, we cannot directly conclude a double unit cell, but we follow the literature and use the  $C_{36}$  double unit cell, given in Ref. 31, which is consistent with our data. The  $Pca2_1$  unit cell consists of two subcells related by a twofold rotation around the  $c$ -axis. For the same sterical reasons, we also apply a double unit cell for  $C_{40}$  and  $C_{44}$ . In the case of  $C_{40}$  and  $C_{44}$  thin films, the symmetry and  $c$ -parameter differ from the  $Pbca$  bulk unit cell that has been found in literature.<sup>2,31,32</sup> The  $c$ -axis of our proposed  $Pca2_1$  orthorhombic unit cell equals the height of two monolayers. In this molecular packing structure, the (001) reflection is forbidden and only *even*-numbered higher order reflections are visible.

TABLE I. Unit cell parameters under the assumption of an orthorhombic cell for the three investigated n-alkanes as determined from the Bragg reflections in the XRR and GIXD data.

|                | $a$                   | $b$                   | $c$                 | $\alpha$   | $\beta$    | $\gamma$   |
|----------------|-----------------------|-----------------------|---------------------|------------|------------|------------|
| $C_{36}H_{74}$ | $4.98(9) \text{ \AA}$ | $7.44(8) \text{ \AA}$ | $95.6 \text{ \AA}$  | $90^\circ$ | $90^\circ$ | $90^\circ$ |
| $C_{40}H_{82}$ | $4.98(9) \text{ \AA}$ | $7.44(8) \text{ \AA}$ | $105.6 \text{ \AA}$ | $90^\circ$ | $90^\circ$ | $90^\circ$ |
| $C_{44}H_{90}$ | $4.98(9) \text{ \AA}$ | $7.44(8) \text{ \AA}$ | $115.2 \text{ \AA}$ | $90^\circ$ | $90^\circ$ | $90^\circ$ |

The Bragg reflection at  $q_z = 1.52(4) \text{ \AA}^{-1}$  denoted with  $(110)_\lambda$  in the XRR graph also appears at exactly the same position in the in-plane measurement. For  $C_{44}$  and  $C_{40}$ , the (002) reflection and its higher orders are also visible in the GIXD graph. Both these findings point to the fact that there must be a co-existing  $90^\circ$  tilted unit cell that we refer to as the lying-down  $\lambda$ -orientation in contrast to the thermodynamically favorable upright-standing  $\sigma$ -orientation.<sup>33</sup>

Both in the XRR and in the GIXD measurements, the Bragg reflections of the  $\lambda$ -orientation are considerably stronger for  $C_{44}$  than in the case of  $C_{40}$  and likewise stronger for  $C_{40}$  than for  $C_{36}$  (see Figure 2(b)). Under the assumption that all three molecules have similar molecular form factors this suggests that longer molecules form a higher percentage of  $\lambda$ -orientation. For shorter n-alkanes with chain-lengths between 23 and 27 carbon atoms, this behavior has been observed before.<sup>32</sup>

The AFM measurements in combination with GIXD scans using various angles of incidence revealed that the biggest amount of  $\lambda$ -orientation is concentrated in the topmost region of the film. At lower angles of incidence corresponding to a smaller penetration depth into the film, the Bragg reflections of the  $\lambda$ -orientation became more dominant compared to the reflections of the  $\sigma$ -orientation. This indicates that the needle-like structures that can be seen on top of the film in the AFM scans are indeed crystallites of  $\lambda$ -orientated molecules. This result is consistent with theoretical findings by Yamamoto *et al.*<sup>33</sup> The AFM-height of these crystallites (100–400 nm) indicates that the absolute number of layers with  $\lambda$ -orientated molecules exceeds the number of layers of the  $\sigma$ -orientation. This explains the strong  $(110)_\lambda$  Bragg reflections in XRR scans as shown in Figure 2(a). The AFM scans shown in Figure 2(c) confirm the findings from the x-ray data and show that  $C_{44}$  forms indeed the highest percentage of  $\lambda$ -orientation while  $C_{36}$  forms the lowest percentage of  $\lambda$ -orientation of the three compared alkanes.

From x-ray rocking scans at the  $(110)_\lambda$  reflection, we can conclude that the  $\lambda$ -orientation consists of crystallites with a high mosaicity ( $\text{FWHM} \gg 1^\circ$ ) as compared to the  $\sigma$ -orientation that exhibits a very low mosaicity in the order of the substrate width ( $\text{FWHM}$  of (002)-reflection  $< 0.03^\circ$ ).<sup>34</sup>

It has been proposed that the higher mobility of shorter n-alkanes makes it easier for them to crystallize into the thermodynamically more favorable  $\sigma$ -orientation. Time-resolved x-ray measurements during growth allow us to follow the growth dynamics and thereby can help to support this conjecture or yield alternative explanations. The suitability of measuring the x-ray reflectivity at the so called anti-Bragg point

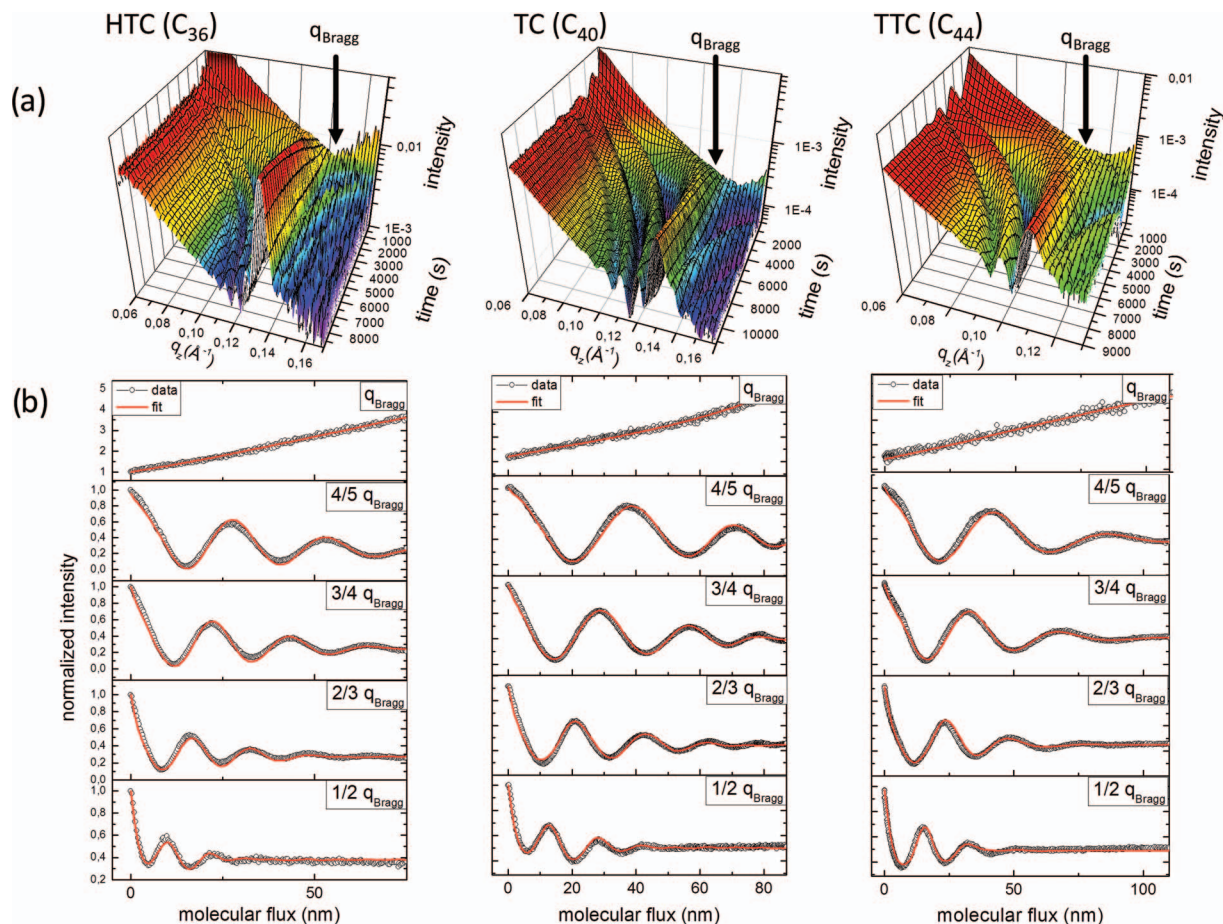


FIG. 3. (a) Evolution of the specular reflectivity as a function of time and  $q_z$  during growth of C<sub>36</sub>, C<sub>40</sub>, and C<sub>44</sub> on oxidized silicon wafers. (b) Cuts through the above 3D graph at fixed  $q_z = 1/2 q_{\text{Bragg}}$ ,  $2/3 q_{\text{Bragg}}$ ,  $3/4 q_{\text{Bragg}}$ ,  $4/5 q_{\text{Bragg}}$ , and  $q_{\text{Bragg}}$  result in experimental growth oscillation shown in black. Red lines show a simultaneous fit at five distinct values of  $q_z$ , using the Trofimov model.

in reciprocal space to study layer-by-layer growth has been demonstrated for several organic systems.<sup>18,35–39</sup>

Layer interference leads to temporal oscillations of the reflected intensity during layer-by-layer growth.<sup>39,40</sup> This can be seen directly from the equation for the reflected intensity  $I_{\text{reflected}}(t)$ , as calculated in kinematic approximation

$$I_{\text{reflected}}(t) = |A_{\text{substrate}}(q_z) \times e^{i\varphi(q_z)} + f(q_z) \times \sum_n \theta_n(t) e^{inq_z d}|^2. \quad (1)$$

$A_{\text{substrate}}(q_z)$ : substrate scattering amplitude,  $f(q_z)$ : molecular form factor,  $\varphi(q_z)$ : phase between substrate and ad-layer scattering,  $n$ : layer number,  $\theta_n$ : fractional coverage of the  $n$ th-layer,  $q_z$ : x-ray wavevector transfer upon reflection, and  $d$ : lattice spacing within the crystalline thin film perpendicular to the substrate surface.

Figure 3 shows the temporal evolution of the x-ray reflectivity of C<sub>36</sub>, C<sub>40</sub>, and C<sub>44</sub>. In the following,  $q_{\text{Bragg}}$  denotes the monolayer-Bragg point at  $q_z = 0.111 \text{ \AA}^{-1}$  for C<sub>36</sub>,  $q_z = 0.121 \text{ \AA}^{-1}$  for C<sub>40</sub>, and  $q_z = 0.134 \text{ \AA}^{-1}$  for C<sub>44</sub>. The monolayer-anti-Bragg point equals the (001)-Bragg-point of the proposed *Pca2*<sub>1</sub> unit cell whose long  $c$ -axis equals the height of two monolayers. Since the (001) reflection is forbidden, no additional scattering intensity from the (001) reflection is observed during the measurement of the anti-Bragg oscillations. From the damping of the intensity oscillations at

the monolayer-anti-Bragg point ( $1/2 q_{\text{Bragg}}$ ) after 4 ML one can conclude the occurrence of a transition from layer-by-layer growth to island growth accompanied by roughening, which is typical for Stranski-Krastanov growth of organic molecules. As the growth proceeds, Laue oscillations develop in the region between the anti-Bragg and Bragg point, indicating a good degree of coherent ordering across the full film thickness. When the temporal intensity oscillations of all three molecules are compared, a chain-length dependence for the growth behavior can be found. In particular, the growth oscillations of the longest molecule C<sub>44</sub> are damped more than the oscillations of C<sub>36</sub> and C<sub>40</sub>, e.g., in the case of C<sub>40</sub> four oscillations are visible at  $2/3 q_{\text{Bragg}}$  while there are only two or three oscillations for C<sub>44</sub>. This suggests that films consisting of the longest molecule C<sub>44</sub> exhibit the fastest roughening.

The quantitative evaluation of real-time x-ray data requires the use of a model describing the growth process to determine the temporal evolution of the layer coverage  $\theta_n(t)$  in Eq. (1). Numerous models have been developed over the last several decades to describe the growth of thin films.<sup>41,42</sup> In contrast to some of the simpler layer-coverage-based models, the growth model developed by Trofimov *et al.*<sup>43–46</sup> allows us, within the assumptions of the model, to extract real, physical parameters such as the ratio of molecular diffusivity to the incident flux of molecules and facilitates comparison of experimental data with theoretical predictions. The main

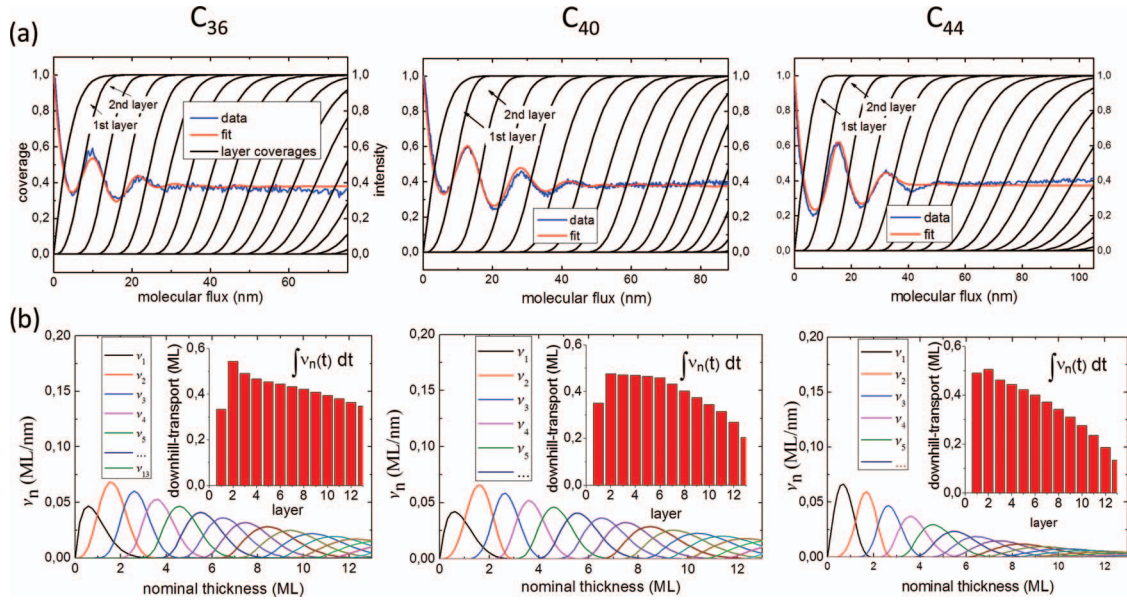


FIG. 4. (a) Layer coverage and (b) downhill-transport rates for  $C_{36}$ ,  $C_{40}$ , and  $C_{44}$  (from left to right). The insets in (b) show the integral downhill-transport for each layer; in other words, the total amount of molecules that are transported from a specific layer into the next lower layer.

assumptions of the Trofimov model are as follows. Complete condensation of evaporated molecules on the surface is assumed (no re-evaporation from the surface). Islands consisting of two or more molecules are assumed to be stable and immobile (only single molecules can diffuse). Furthermore, uphill-transport, long-range interactions, and multilayer diffusion, e.g., molecules diffusing directly from the 3rd into the 1st layer, are excluded. In this way, the amount of parameters needed to describe the growth and nucleation process can be reduced significantly. In this work, we apply the Trofimov model to fit the x-ray reflectivity simultaneously at 5 distinct points of reciprocal space, namely, at  $1/2 q_{Bragg}$ ,  $2/3 q_{Bragg}$ ,  $3/4 q_{Bragg}$ ,  $4/5 q_{Bragg}$ , and  $q_{Bragg}$  (see Figure 3(b)).

As we are concerned only with out-of-plane structure, we use a simplified version of the original Trofimov model, describing the growth process only via the growth rate  $R_n$  and the *effective* critical layer coverage of each layer as shown in Eq. (2)–(4). This version of the Trofimov model has already been successfully applied to the growth of pentacene and diindenoperylene.<sup>47</sup> The critical layer coverage of the  $n$ th layer  $\theta_{n,cr}$  gives the coverage  $\theta_n$  of a layer before the  $n+1$ th layer starts to nucleate and grow on top of the  $n$ th layer.<sup>48</sup> The feeding zone parameter  $\xi_n$  marks the size (in units of normalized coverage) of the zone on top of the  $n$ th layer where molecules will contribute to nucleation and growth of the  $n+1$ th layer as opposed to the region outside the feeding zone where molecules will diffuse over the edge into the  $n$ th layer (see Figure 1(c)),

$$\frac{d\theta_n}{dt} = \begin{cases} R_1(1 - \theta_1) + R_{n>1}(\theta_1 - \xi_1), & n = 1, \\ R_{n>1}(\xi_{n-1} - \xi_n), & n > 1, \end{cases} \quad (2)$$

with the size of the feeding zone given by

$$\xi_n = \begin{cases} 0, & \theta_n < \theta_{n,cr} \\ 1 - e^{-[\sqrt{-\ln(1-\theta_n)} - \sqrt{-\ln(1-\theta_{n,cr})}]^2}. \end{cases} \quad (3)$$

The critical layer coverage parameters in Eq. (3) are calculated via

$$\theta_{n,cr} = \theta_{2,cr} e^{(-n-2)/N_c}, \quad \text{for } n > 2. \quad (4)$$

The fit of only the anti-Bragg oscillations is in some cases overdetermined by the seven fit parameters, that is, the fit parameters could be ambiguous. Fitting simultaneously at five distinct points in reciprocal space simultaneously restricts the range of the fit parameters and therefore gives a better estimate. Besides, additional information is contained within the oscillations closer to the Bragg reflection. At  $1/2 q_{Bragg}$ , the oscillations are completely damped after about 4 ML and no information about the growth dynamics beyond that point can be extracted. But at  $q_z$ -values closer to the Bragg reflection like  $4/5 q_{Bragg}$  the XRR intensity keeps on oscillating, yielding information about the critical layer coverage and growth rate up to thicknesses of 10–20 ML.

Two slightly different sticking coefficients for the first monolayer adsorbed directly on the substrate and all subsequent layers have been introduced to take different substrate-molecule and molecule-molecule interaction mechanisms into account,<sup>49</sup> while for  $C_{40}$  a slightly accelerated growth rate for higher layers has been put into the model to deal with the changing growth oscillation periodicity towards the end of the growth. The layer thickness parameter  $d$  in Eq. (1) has been kept constant, that is, the molecular tilt angle is assumed not to change. The fitted layer coverage can be seen in Figure 4(a), also indicating a stronger layer-by-layer growth behavior in the early stages of the growth. In the later stages of the growth many layers get filled at the same time, indicating island growth and roughening.

For a quantitative comparison of the growth behavior of the three molecules, we compare physical parameters derived from the fitted layer coverage, such as the amount of molecules diffusing from one layer into lower layers during growth. The downhill-transport rate  $v_n(t) = [\theta_n(t)$

–  $\xi_n(t)] \times R_n$ , shown in Figure 4(b), describes the amount (in ML) of molecules diffusing from the  $n + 1$ th into the  $n$ th layer per time interval.

The total amount of molecules diffusing from the  $n + 1$ th into the  $n$ th layer is shown in the insets in Figure 4(b). In the case of  $C_{36}$  and  $C_{40}$ , a rather small critical layer coverage ( $<20\%$ ) of the first monolayer yields a comparatively small downhill-transport from the second into the first layer. For  $C_{44}$ , the first two layers grow in a smoother way, indicated by a larger downhill-transport from the second to the first layer. After growth of about 5 ML, the integral downhill-transport of the longer molecules drops below the integral downhill-transport of the shorter molecules. This chain-length dependence becomes even more significant as the growth proceeds. For thicknesses above 10 ML, the integral downhill-transport of  $C_{36}$  exceeds the integral downhill-transport of  $C_{44}$  by about 60% (see Figure 4(b)). This indicates that the length of a molecule is crucial for its interlayer-transport properties, particularly within the roughening regime.

The small critical layer coverage parameters ( $<0.3$ ) that have been derived for all three molecules indicate a substantial Ehrlich-Schwoebel barrier, limiting the downhill-transport probability.<sup>15</sup> The probability of molecules diffusing from the  $n + 1$ th layer into the  $n$ th layer is in this case related to the Ehrlich-Schwoebel barrier  $E_{ES}$  as follows:

$$p_n(t) = \frac{v_n(t)}{R_n \times [\theta_n(t) - \theta_{n+1}(t)]} \propto A_n(t) \times e^{-E_{ES}/kT} \quad (5)$$

with  $A_n$  being a factor depending on the island perimeters and the diffusivity of the molecules.<sup>16,50,51</sup> Averaging the time-dependent probability of Eq. (5) by integrating from the beginning of the growth of the  $n$ th layer  $t(\theta_n = 0)$  to the filling of the  $n+1$ th layer  $t(\theta_{n+1} = 1)$  and dividing by the time interval makes it possible to simplify the above relation to

$$\overline{p}_n \propto \overline{A}_n \times e^{-E_{ES}/kT}, \quad (6)$$

where  $\overline{p}_n$  denotes the *mean* downhill-transport probability. According to this, and for film thicknesses above 5 ML, the mean probability of downhill-transport is about 34% for  $C_{36}$ , 31% for  $C_{40}$ , and only 28% for the longest molecule,  $C_{44}$ .

While the *absolute* value for  $E_{ES}$  is not easy to establish reliably, we can estimate the *differences* of  $E_{ES}$  between the different chains, namely,  $C_{36}$ ,  $C_{40}$ , and  $C_{44}$ , assuming that they can all be similarly well described by our model. Furthermore, we assume that the island perimeters and intra-layer diffusion barriers, and thus the prefactors  $\overline{A}_n$  are similar for all three molecules. According to this estimate and for film thicknesses  $>5$  ML,  $C_{40}$  molecules hopping from one layer into the next lower have to overcome an Ehrlich-Schwoebel barrier that exceeds the corresponding Ehrlich-Schwoebel barrier of  $C_{36}$  by about  $\Delta E_{ES} = 2$  meV (i.e.,  $E_{ES}(C_{40}) - E_{ES}(C_{36}) = 2$  meV), while  $C_{44}$  molecules have to overcome a barrier that exceeds the barrier of  $C_{36}$  by approximately  $\Delta E_{ES} = 5$  meV ( $E_{ES}(C_{44}) - E_{ES}(C_{36}) = 5$  meV). In other words, in this regime the increase of the Ehrlich-Schwoebel barrier per additional carbon atom is of the order of 0.5 meV under the above approximations.

The chain-length dependent downhill-transport and the chain-length dependent percentage of  $\lambda$ -orientation in the top-

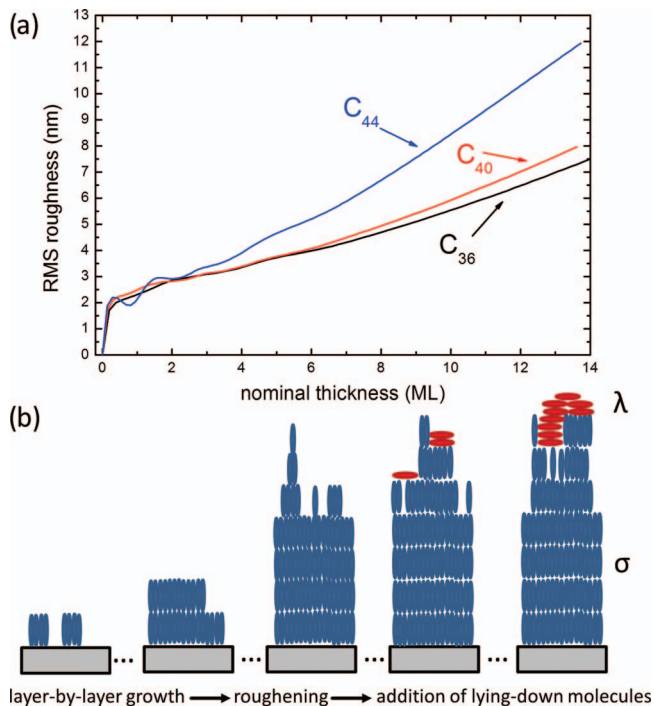


FIG. 5. (a) Evolution of the interface roughness during growth of  $C_{36}$ ,  $C_{40}$ , and  $C_{44}$  and (b) sketch of the transition of the growth mode and the formation of  $\lambda$ -orientation within the topmost region of the film.

most region of the film suggest that there might also be a chain-length dependence of the film roughness. The root-mean-square roughness of the film can be calculated directly from the layer coverage as given by the Trofimov model fit via

$$\sigma(t) = \sqrt{\sum_{n=0}^{\infty} (\theta_n(t) - \theta_{n+1}(t)) [d \times n - \bar{d}(t)]^2} \quad (7)$$

with  $\theta_n(t)$  being the fractional coverage of the  $n$ th layer,  $d$  the lattice spacing, and  $\bar{d}(t)$  being the nominal film thickness.<sup>52</sup> In Figure 5(a), the roughness evolution during thin film growth is shown for all three molecules.  $C_{44}$  exhibits the smoothest layer-by-layer growth during the first two monolayers, indicated by oscillations of the roughness evolution. After evaporation of about 4 ML there is a strong increase of roughness. Despite the smooth growth in the beginning,  $C_{44}$  exhibits by far the fastest roughening after 4 ML, and  $C_{40}$  roughens faster than  $C_{36}$ , but the differences between the latter two are within our error bars. Therefore, we conclude that the observed chain-length dependent roughening is a consequence of the chain-length dependent interlayer-transport properties and Ehrlich-Schwoebel barriers. This behavior is different from the corresponding chain-length dependent behavior in the case of small molecules where shorter chains form more disordered structures. In the past, simulations have shown that, indeed, a greater downhill-transport is expected to support layer-by-layer growth while a smaller downhill-transport of molecules probably leads to faster roughening.<sup>35</sup> Nevertheless, in order to get a thorough understanding of the molecular kinetics governing the growth process, additional real-time studies are required, e.g., measurements of the in-plane island perimeters, performed at different temperatures, to determine reliable *absolute* values of  $E_{ES}$ .

#### IV. CONCLUSIONS

A comparative real-time and *in situ* growth study of the three n-alkanes C<sub>36</sub>, C<sub>40</sub>, and C<sub>44</sub> on SiO<sub>2</sub> has been performed using energy dispersive real-time x-ray reflectivity. It has been shown that structural properties of organic thin films consisting of chain-like molecules can be tuned significantly by varying the number of chain segments. While all three molecules align mostly in upright-standing geometry, longer molecules form more crystallites of lying-down molecules in the top-most region of the film.

Furthermore, films made of longer molecules exhibit faster roughening than films consisting of shorter molecules. This can be explained by the chain-length dependence of the downhill-transport rates during the growth. The amount of molecules diffusing from one layer into the next lower layer decreases with increasing chain-length of the molecules. Assuming that the thermal activation over the Ehrlich-Schwoebel barrier limits the downhill-transport probability during the later stages of the growth,<sup>15,50</sup> we conclude from the derived downhill-transport rates that there must also be a chain-length dependence of the Ehrlich-Schwoebel barrier, with longer molecules having a higher energy barrier to overcome when diffusing from one layer into the next lower layer. This would be in agreement with simulations for several organic molecules performed by Goose *et al.*<sup>17</sup>

Our results show that it is preferable to use shorter molecules for any application where a smooth interlayer is required and coexistence of two different molecular orientations (lying-down/upright-standing) has to be avoided.

#### ACKNOWLEDGMENTS

Financial support from “Deutsche Forschungsgemeinschaft” (DFG) via Grant No. schr700/13-1 is gratefully acknowledged. We would also like to thank the Helmholtz-Zentrum Berlin for access to the EDR beamline at BESSY II.

- <sup>1</sup>C. Merkl, T. Pföhl, and H. Riegler, *Phys. Rev. Lett.* **79**, 4625–4628 (1997).
- <sup>2</sup>S. R. Craig, G. P. Hastie, K. J. Roberts, and J. N. Shenvood, *J. Mater. Chem.* **4**, 977–981 (1994).
- <sup>3</sup>A. Holzwarth, S. Loporatti, and H. Riegler, *EPL* **52**, 653–659 (2000).
- <sup>4</sup>C. W. Frank, V. Rao, M. M. Despotopoulou, R. F. W. Pease, W. D. Hinsberg, R. D. Miller, and J. F. Rabolt, *Science* **273**, 912–915 (1996).
- <sup>5</sup>M. Kraus, S. Richler, A. Opitz, W. Brütting, S. Haas, T. Hasegawa, A. Hinderhofer, and F. Schreiber, *J. Appl. Phys.* **107**, 094503 (2010).
- <sup>6</sup>F. Schreiber, *Prog. Surf. Sci.* **65**, 151–256 (2000).
- <sup>7</sup>M. Kind and C. Wöll, *Prog. Surf. Sci.* **84**, 230–278 (2009).
- <sup>8</sup>M. Kraus, S. Haug, W. Brütting, and A. Opitz, *Org. Electron.* **12**, 731–735 (2011).
- <sup>9</sup>G. Ungar, *J. Phys. Chem.* **197**, 689–695 (1983).
- <sup>10</sup>N. Wentzel and S. T. Milner, *J. Chem. Phys.* **132**, 044901 (2010).
- <sup>11</sup>F. Tao and S. L. Bernasek, *Chem. Rev.* **107**, 1408–1453 (2007).
- <sup>12</sup>M. Atkinson and M. Richardson, *Trans. Faraday Soc.* **65**, 1749–1763 (1968).
- <sup>13</sup>N. G. Almarza, E. Enciso, and F. J. Bermejo, *J. Chem. Phys.* **96**, 4625–4632 (1992).
- <sup>14</sup>M. Mondello, G. S. Grest, E. B. Webb, and P. Peczak, *J. Chem. Phys.* **109**, 798–805 (1998).

- <sup>15</sup>R. L. Schwobel and E. J. Shipsey, *J. Appl. Phys.* **37**, 3682–3686 (1966).
- <sup>16</sup>G. Hlawacek, P. Puschnig, P. Frank, A. Winkler, C. Ambrosch-Draxl, and C. Teichert, *Science (N.Y.)* **321**, 108–111 (2008).
- <sup>17</sup>J. E. Goose, E. L. First, and P. Clancy, *Phys. Rev. B* **81**, 10–12 (2010).
- <sup>18</sup>B. Krause, A. C. Dürr, F. Schreiber, H. Dosch, and O. H. Seeck, *J. Chem. Phys.* **119**, 3429–3435 (2003).
- <sup>19</sup>H. Proehl, R. Nitsche, T. Dienel, K. Leo, and T. Fritz, *Phys. Rev. B* **71**, 1–14 (2005).
- <sup>20</sup>U. Heinemeyer, K. Broch, A. Hinderhofer, M. Kytka, R. Scholz, A. Gerlach, and F. Schreiber, *Phys. Rev. Lett.* **104**, 1–4 (2010).
- <sup>21</sup>T. Hosokai, A. Gerlach, A. Hinderhofer, C. Frank, G. Ligorio, U. Heinemeyer, A. Vorobiev, and F. Schreiber, *Appl. Phys. Lett.* **97**, 063301 (2010).
- <sup>22</sup>M. Hanke, V. M. Kaganer, O. Bierwagen, M. Niehle, and A. Trampert, *Nanoscale Res. Lett.* **7**, 203 (2012).
- <sup>23</sup>S. Kowarik, A. Gerlach, S. Sellner, L. Cavalcanti, and F. Schreiber, *Adv. Eng. Mater.* **11**, 291–294 (2009).
- <sup>24</sup>B. F. Macdonald, R. J. Cole, and V. Koutsos, *Surf. Sci.* **548**, 41–50 (2004).
- <sup>25</sup>S. Kowarik, A. Gerlach, and F. Schreiber, *J. Phys.: Condens. Matter* **20**, 184005 (2008).
- <sup>26</sup>Y. Kim, H. L. Strauss, and R. G. Snyder, *J. Phys. Chem.* **93**, 7520–7526 (1989).
- <sup>27</sup>K. A. Ritley, B. Krause, F. Schreiber, and H. Dosch, *Rev. Sci. Instrum.* **72**, 1453–1457 (2001).
- <sup>28</sup>F. Neissendorfer, U. Pietsch, and G. Brezesinski, *Meas. Sci. Technol.* **10**, 354–361 (1999).
- <sup>29</sup>U. Pietsch, J. Grenzer, T. Geue, F. Neissendorfer, G. Brezesinski, C. Symietz, H. Möhwald, and W. Gudat, *Nucl. Instrum. Methods Phys. Res. A* **467–468**, 1077–1080 (2001).
- <sup>30</sup>S. Kowarik, A. Gerlach, W. Leitenberger, J. Hu, G. Witte, C. Wöll, U. Pietsch, and F. Schreiber, *Thin Solid Films* **515**, 5606–5610 (2007).
- <sup>31</sup>P. W. Teare, *Acta Crystallogr.* **12**, 294–300 (1959).
- <sup>32</sup>K. Nozaki, R. Saihara, K. Ishikawa, and T. Yamamoto, *Jpn. J. Appl. Phys., Part 1* **46**, 761–769 (2007).
- <sup>33</sup>T. Yamamoto, K. Nozaki, A. Yamaguchi, and N. Urakami, *J. Chem. Phys.* **127**, 154704 (2007).
- <sup>34</sup>See supplementary material at <http://dx.doi.org/10.1063/1.4719530> for rocking scans of the  $\lambda$ - and  $\sigma$ -orientation.
- <sup>35</sup>B. Krause, F. Schreiber, H. Dosch, A. Pimpinelli, and O. H. Seeck, *EPL* **65**, 372–378 (2004).
- <sup>36</sup>S. Kowarik, A. Gerlach, S. Sellner, F. Schreiber, L. Cavalcanti, and O. Kononov, *Phys. Rev. Lett.* **96**, 1–4 (2006).
- <sup>37</sup>A. Hinderhofer, A. Gerlach, S. Kowarik, F. Zontone, J. Krug, and F. Schreiber, *EPL* **91**, 56002 (2010).
- <sup>38</sup>A. Gerlach, S. Sellner, S. Kowarik, and F. Schreiber, *Phys. Status Solidi A* **205**, 461–474 (2008).
- <sup>39</sup>A. Mayer, R. Ruiz, H. Zhou, R. Headrick, A. Kazimirov, and G. Malliaras, *Phys. Rev. B* **73**, 1–5 (2006).
- <sup>40</sup>S. Kowarik, A. Gerlach, M. W. Skoda, S. Sellner, and F. Schreiber, *Eur. Phys. J. Spec. Top.* **167**, 11–18 (2009).
- <sup>41</sup>P. Cohen, G. Petrich, P. Pukite, and G. Whaley, *Surf. Sci.* **216**, 222–248 (1989).
- <sup>42</sup>W. Braun, B. Jenichen, V. M. Kaganer, A. G. Shtukenberg, L. Däweritz, and K. H. Ploog, *Surf. Sci.* **525**, 126–136 (2003).
- <sup>43</sup>V. I. Trofimov, V. G. Mokerov, and A. G. Shumyankov, *Thin Solid Films* **306**, 105–111 (1997).
- <sup>44</sup>V. I. Trofimov and H. S. Park, *J. Korean Phys. Soc.* **40**, 344–348 (2002).
- <sup>45</sup>V. I. Trofimov and V. G. Mokerov, *Thin Solid Films* **428**, 66–71 (2003).
- <sup>46</sup>V. I. Trofimov, *Thin Solid Films* **428**, 56–65 (2003).
- <sup>47</sup>A. R. Woll, T. V. Desai, and J. R. Engstrom, *Phys. Rev. B* **84**, 1–16 (2011).
- <sup>48</sup>J. Tersoff, A. W. Denier van der Gon, and R. M. Tromp, *Phys. Rev. Lett.* **72**, 266–270 (1994).
- <sup>49</sup>A. Amassian, T. V. Desai, S. Kowarik, S. Hong, A. R. Woll, G. G. Malliaras, F. Schreiber, and J. R. Engstrom, *J. Chem. Phys.* **130**, 124701 (2009).
- <sup>50</sup>G. Ehrlich and F. G. Hudda, *J. Chem. Phys.* **44**, 1039–1049 (1966).
- <sup>51</sup>R. L. Schwobel, *J. Appl. Phys.* **40**, 614 (1969).
- <sup>52</sup>S. Kowarik, A. Gerlach, A. Hinderhofer, S. Milita, F. Borgatti, F. Zontone, T. Suzuki, F. Biscarini, and F. Schreiber, *Physica Status Solidi (RRL)* **2**, 120–122 (2008).